Supporting Information:

Polymer Infused Porous Surfaces for Robust, Thermally Conductive, Self-Healing Coatings for Dropwise Condensation

Kyle L. Wilke[1], Dion S. Antao[1,†], Samuel Cruz[1], Ryuichi Iwata[1], Yajing Zhao[1], Arny Leroy[1], Daniel J. Preston[1,††], Evelyn N. Wang[1,]*

[1]Department of Mechanical Engineering, Massachusetts Institute of Technology, Cambridge, MA 02139, USA

Present Addresses

[†]J. Mike Walker '66 Department of Mechanical Engineering, Texas A&M University, College Station, TX 77843, USA

[††]Department of Mechanical Engineering, Rice University, 6100 Main St., Houston, TX 77005, USA

S1. Designing Polymer Infused Porous Surfaces (PIPS)

To achieve durable condensation heat transfer enhancement through dropwise condensation with low-surface-energy coatings, multiple design criteria for the proposed PIPS were considered. The first is that the coating must not add significant resistance to heat transfer, *i.e.*, the thermal resistance must be low. Thermal resistance scales as H/k, where k and H are the thermal conductivity and the thickness of the coating, respectively. Historically, because low-surface-

energy coatings tend to have low thermal conductivity, low resistance has been achieved by using very thin coatings ($H < 4$ μm). At these small thicknesses, adhesion of polymers is poor, resulting in inadequate robustness. Therefore, improving adhesion of the coating, as well as improving thermal conductivity such that thicker coatings may be used would both benefit coating lifetime and heat transfer performance. Second is the ability of the low-surface-energy coating to promote dropwise condensation, for which the wetting behavior on the surface is important. Generally, the quality and performance of dropwise condensation is greatest when the advancing contact angle, θ_a, is large ($\theta_a > 90$ degrees) and the contact angle hysteresis, *i.e.*, the difference between the advancing contact angle and the receding contact angle, is small ($\theta_a - \theta_r < 20$ degrees).[1] In this section we step through the design rationale for surface types chosen in this study.

PIPS form a composite material consisting of low thermal conductivity polymer and a higher thermal conductivity nanostructure, and the composite material has a surface composed of highly wetting nanostructure and hydrophobic polymer. Therefore, any nanostructure exposed at the surface will affect the wettability of the surface, which would affect the quality of dropwise condensation. Previous works have developed expressions for the expected advancing and receding contact angles of composite surfaces, θ_a and θ_r, respectively

$$\cos\theta_a = \cos\theta_{polymer} \tag{S1}$$

$$cos\,\theta_r = \sqrt{1-\phi(x=0)}\,cos\,\theta_{polymer} + \left(1-\sqrt{1-\phi(x=0)}\right)\cos\theta_{ns} \tag{S2}$$

where $\phi(x=0)$ is the nanostructure solid fraction of the nanostructure at the surface exposed to the liquid and $\theta_{polymer}$ and θ_{ns} are the contact angle of the polymer and nanostructure material, respectively.[2] In order to minimize contact angle hysteresis, solid fraction of the nanostructure at the surface should remain small (Figure S1b). We note that there is also the possibility to overfill the nanostructure with polymer, thereby creating a polymer only surface. However, because the

overfilled polymer would have low thermal conductivity, it would create significant resistance to heat transfer and should be kept thin. Therefore, in this work, we avoid overfilling and instead design the surface such that the nanostructure solid fraction is low enough that contact angle hysteresis is less than 20 degrees ($\phi(x = 0) < 0.4$).

The network of nanostructure inside the polymer also enhances the thermal conductivity. In fact, because the nanostructure is grown on the surface, it inherently creates a continuous, percolated network of high thermal conductivity material through the entire thickness of the layer, forming parallel heat transfer paths. In this scenario, the effective thermal conductivity, $k_{eff,}$ of the layer can be estimated as[3-5]

$$k_{eff}(x) = \phi(x)k_{ns} + \big(1 - \phi(x)\big)k_{polymer} \tag{S3}$$

where k_{ns} and $k_{polymer}$ are the thermal conductivities of the nanostructure and polymer, respectively, and x is the location within the layer with $x = 0$ located at the exposed surface. To start, in Figure S1b, we consider nanostructures with constant nanostructure solid fraction throughout the layer thickness made of copper ($k_{ns} = 386$ W/mK). Effective thermal conductivity can be enhanced orders of magnitude over that of the polymer ($k_{polymer} = 0.29$ W/mK) even with relatively small solid fractions of nanostructure. Therefore, a balance exists between the thermal conductivity enhancement and the contact angle hysteresis, motivating the use of nanostructures with intermediate solid fractions.

To enhance adhesion of polymers to a surface, surfaces are often roughened, increasing the total surface area the polymer is in contact with as well as enabling mechanical interlocking of the surface and polymer.[6-8] In the case of pillars, the surface area enhancement is used as a proxy to adhesion to guide design choices.

$$\text{Surface Area Enhancement} = \frac{L^2 + \pi DH}{L^2} \tag{S4}$$

where L is the pitch and D is the diameter of the pillar, as shown in Figure S1a. The surface area enhancement is shown in Figure S1c for different nanostructure solid fractions, ϕ (for pillars $\phi = (\pi D^2/4)/L^2$), and a height of 10 μm. H = 10 μm was chosen as a representative case given thickness should remain relatively small to limit the thermal resistance the coating adds. The surface area enhancement in this scenario was maximized by moving to smaller pitch, *i.e.*, tall slender structures, where significant enhancement is only reached when structure pitch is hundreds of nanometers. Therefore, this work used nanostructures, however, it is expected that other strategies, such as microstructures, could achieve similar performance. Cross hatch adhesion testing was conducted according to ASTM D3359 to confirm high adhesion of the PIPS layer (Figure S8), with no peeling observed.

However, given many nanostructures do not form a constant nanostructure solid fraction throughout the thickness, we considered the effect of varied nanostructure solid fraction throughout the coating. We considered three scenarios—constant, linear, and parabolic nanostructure solid fractions (ϕ) throughout the layer—where $k_{eff}(x)$ is shown along x (Figure S2). For the constant nanostructure solid fraction, we use $\phi = 0.3$ as it falls within the middle of our expected target range from Figure S1b, whereas for linear and parabolic nanostructure solid fractions we assume $\phi(x = 0) = 0$ and $\phi(x = H) = 1$, where *x=0* represents the surface exposed to condensate and *x=H* represents the base of the nanostructure.

The resulting average effective conductivity, k_{eff}, of the entire coating, *i.e.*, the effective conductivity if the coating was treated as a homogeneous medium along x, is labeled in Figure S2 for these scenarios with copper nanostructures. All types of nanostructure greatly enhanced the thermal conductivity over the polymer; however, constant nanostructure solid fraction is most

effective, followed by linear, and then parabolic. Parabolic performs the worst due to the small amount of nanostructure near $x = 0$, resulting in a low effective thermal conductivity.

Based on the calculated effective thermal conductivities, we define a critical thickness, H_{crit}, beyond which the coating would degrade dropwise heat transfer performance by 10 percent or more, *i.e.*, a significant degradation of performance. This critical thickness was estimated using a thermal resistance network

$$\frac{1.1}{h_{drop}} = \frac{1}{h_{drop}} + \frac{H_{crit}}{k_{eff}} \quad \text{(S5)}$$

where h_{drop} is the heat transfer coefficient of dropwise condensation. We take an estimated value of h_{drop} = 133 kW/m^{2}K. 133 kW/m^{2}K was used in this case based on correlations by Rose at experimental conditions used in this study.[9] The resulting critical thicknesses, effective thermal conductivities, surface nanostructure solid fraction, and the expected contact angle hysteresis are shown in Table S1 for different nanostructure solid fractions and materials. Without using nanostructures, Teflon AF coatings can only be 0.22 μm thick before reducing condensation heat transfer by more than 10%, highlighting the strict design constraints on these coating types. Adding high thermal conductivity copper nanostructures increased this critical thickness significantly without increasing contact angle hysteresis beyond 20 degrees, whereas adding a lower thermal conductivity nanostructure such as copper oxide increased the critical thickness significantly less than copper but still provided an improvement over the polymer. To prove the validity and flexibility of PIPS, two designs were chosen and are highlighted in blue in the table. Parabolic copper oxide nanostructures with H = 1.5 μm, based on copper oxide nanoblades,[10] and copper pillars with a nanostructure solid fraction of 0.4 and two thickness, H = 5 and 20 μm, were used.

S2. Heat transfer measurement

To determine the condensation heat flux and condenser surface temperature, we recorded temperatures at evenly-spaced thermocouples mounted within the copper condenser block; we input these temperatures into the 1-dimensional form of Fourier's law to determine the heat flux, and, from a corresponding thermal resistance network for the copper block, the surface temperature was determined. The copper block was insulated with a polyetherimide sleeve to minimize heat transfer at the sidewalls, shown in Figure 3a in the main text. In order to justify the use of the 1-dimensional Fourier's law in this case, we created a COMSOL model of the insulated copper condenser block (Figure S3). The resulting temperature profile was confirmed to be highly linear, allowing use of the 1-dimensional form of Fourier's law to determine heat flux.

S3. Expected dropwise heat transfer performance with PIPS resistance

The PIPS coating adds a thermal resistance, thus lowering the expected performance compared to dropwise condensation without PIPS. Using a serial thermal resistance model, we can model the expected performance as

$$\frac{1}{h_{expected}} = \frac{1}{h_{drop}} + \frac{H_{PIPS}}{k_{eff}} \tag{S6}$$

where H_{PIPS} is the thickness of the PIPS layer, h_{drop} is the dropwise heat transfer coefficient (133 kW/m^{2}K is used in this case based on correlations by Rose[9]), and h_{expected} is the performance including the PIPS layer, which is plotted in Figure 3b.

S4. Contact angle hysteresis, nucleation density, and heat transfer coefficient

If polymer is removed from the PIPS during condensation and nanostructure is gradually exposed or if degradation at the surface increases roughness, the wettability of the surface will change, where the equation for the receding contact angle must account for the exposed

nanostructure or increased roughness (inset of Figure S4). To model the expected behavior, we add a roughness factor, *r*, to Eq. S2 to account for exposed nanostructures increasing the surface area above that of the nanostructure solid fraction,

$$cos\,\theta_r = \sqrt{1-\phi(x=0)}\,cos\,\theta_{polymer} + r\left(1-\sqrt{1-\phi(x=0)}\right)\cos\theta_{ns} \tag{S7}$$

For the pillar nanostructures shown in Figure S1a, this roughness factor can be estimated by

$$r = \frac{\frac{\pi D^2}{4} + \pi DX}{\frac{\pi D^2}{4}} \tag{S8}$$

where *X* is the length of exposed pillar/nanostructure. In Figure S4, the expected hysteresis is shown as the roughness factor is increased for two nanostructure solid fractions. The higher solid fraction has a significantly higher increase in hysteresis as the nanostructure is exposed. We attribute the higher nanostructure solid fraction to be the primary reason Cu nanowire PIPS had observable hysteresis increase after testing, while Cu nanoblade PIPS did not.

This increase in contact angle hysteresis can be translated to expected heat transfer performance degradation using previously developed models that connect hysteresis to the droplet size distribution on the surface. The heat transfer rate through a single droplet of radius *r* on a flat hydrophobic surface can be calculated by:[11]

$$q(r) = \frac{\pi r^2(\Delta T - \frac{2T_{\mathrm{v}}\sigma}{r h_{\mathrm{fg}}\rho_{\mathrm{w}}})}{\frac{1}{2h_{\mathrm{i}}(1-\cos\theta_a)} + \frac{r\theta_a}{4k_{\mathrm{w}}\sin\theta_a} + \frac{\delta}{k_{\mathrm{HC}}\sin^2\theta_a}} \tag{S9}$$

where ΔT is the subcool (temperature difference between vapor and condensing surface), T_{v} is vapor temperature; σ, h_{fg}, ρ_{w}, and k_{w} are surface tension, latent heat, density and thermal conductivity of the condensing fluid; θ_a is the advancing contact angle of the condensing fluid on the condenser surface. The term $\frac{\delta}{k_{\mathrm{HC}}\sin^2\theta_a}$ represents the thermal resistance of the hydrophobic

coating, where δ and k_{HC} are the thickness and the thermal conductivity of the hydrophobic coating, respectively. In order to focus on the effects of the contact angle hysteresis on the dropwise condensation heat transfer performance, we start by assuming negligible thermal resistance of the hydrophobic coating. h_{i} is the interfacial condensation heat transfer coefficient, which can be calculated by[12]

$$h_{\mathrm{i}} = \frac{2\alpha}{2-\alpha}\frac{\rho_{\mathrm{v}} h_{\mathrm{fg}}^2}{T_{\mathrm{sat}}\sqrt{2\pi R_{\mathrm{g}} T_{\mathrm{sat}}}} \tag{S10}$$

where α is the condensation coefficient, which is the ratio of vapor molecules that will be captured by the liquid phase to the total number of vapor molecules reaching the liquid surface ($0 \ll \alpha \ll 1$). We assumed $\alpha = 1$, which is appropriate for clean environments such as the environmental chamber with negligible non-condensable gases. ρ_{v} and T_{sat} are the density and the temperature of the saturated vapor. R_{g} is the specific gas constant of the condensing fluid (461.5 J/kgK for water).

The heat flux averaged over the whole condensing surface can be derived from integrating the heat transfer through each individual droplet while considering the droplet size distribution[11]

$$q = \int_{r_{min}}^{r_e} q(r)n(r)dr + \int_{r_e}^{r_{max}} q(r)N(r)dr \tag{S11}$$

where r_{min}, the minimum viable drop radius, which is usually on the order of 1 nm and is a function of the surface subcool ΔT,[13] is

$$r_{min} = \frac{2T_v\sigma}{h_{fg}\rho\Delta T} \tag{S12}$$

The boundary between the small droplets (droplets which primarily grow by themselves without coalescing with other droplets) and the large droplets (droplets whose growth is dominated by coalescence) is set by r_e. The value of r_e can be determined by experimental characterization and

is usually on the order of 1 μm. For randomly distributed droplets, r_e can be related to the nucleation density N_s, *i.e.*, the number of nucleation sites per unit area of condensing surface[11]

$$r_e = \frac{1}{\sqrt{4N_s}} \tag{S13}$$

Experimental values of droplet nucleation density N_s with a range from 10^9/m^2 to 10^{15}/m^2 have been used in previous literature,[14] and in the case of PIPS, may be influenced by any exposed nanostructure as well as degradation over time.

The maximum droplet radius, r_{max}, can be measured from experiments or estimated by the force balance between surface tension and gravity. r_{max} is usually on the order of 1 mm for water. An explicit expression for r_{max} considering contact angle hysteresis can be derived as[12]

$$r_{max} = \left(\frac{6(\cos\theta_r - \cos\theta_a)\sin\theta_e \sigma}{\pi(2 - 3\cos\theta_e + \cos{\theta_e}^3)\rho g \cos\Theta}\right)^{0.5} \tag{S14}$$

where θ_e is the static contact angle and can be calculated by $\theta_e = \cos^{-1}(0.5\cos\theta_a + 0.5\cos\theta_r)$. Θ is the surface inclination from the vertical, where $\Theta = 0$ for vertical condensing surface.

$n(r)$ and $N(r)$ in Eq. S11 refer to droplet size distribution for the small droplets and the large droplets, respectively. $n(r)$ can be analytically solved by[11]

$$n(r) = \frac{1}{3\pi r_e^3 r_{max}} \left(\frac{r_e}{r_{max}}\right)^{-\frac{2}{3}} \frac{r(r_e - r_{min})}{r - r_{min}} \frac{A_2 r + A_3}{A_2 r_e + A_3} exp(B_1 + B_2) \tag{S15}$$

where

$$A_1 = \frac{\Delta T}{\rho_w h_{fg}(1 - \cos\theta_a)^2(2 + \cos\theta_a)} \tag{S16}$$

$$A_2 = \frac{\theta_a}{4k_w \sin\theta_a} \tag{S17}$$

$$A_3 = \frac{1}{2h_i(1 - \cos\theta_a)} + \frac{\delta}{k_{HC}\sin^2\theta_a} \tag{S18}$$

$$B_1 = \frac{A_2}{\tau A_1}\left[\frac{r_e^2 - r^2}{2} + r_{min}(r_e - r) - r_{min}^2\, ln\left(\frac{r - r_{min}}{r_e - r_{min}}\right)\right] \quad \text{(S19)}$$

$$B_2 = \frac{A_3}{\tau A_1}\left[(r_\mathrm{e} - r) - r_\mathrm{min} \ln\left(\frac{r - r_\mathrm{min}}{r_\mathrm{e} - r_\mathrm{min}}\right)\right] \quad \text{(S20)}$$

$$\tau = \frac{3r_\mathrm{e}^2(A_2 r_\mathrm{e} + A_3)^2}{A_1(11A_2 r_{\mathrm{e}2} - 14A_2 r_\mathrm{e} r_\mathrm{min} + 8A_3 r_\mathrm{e} - 11A_3 r_\mathrm{min})} \quad \text{(S21)}$$

For large droplets whose growth rate is dominated by droplet coalescence, droplet size distribution can be expressed as[15]

$$\mathrm{N}(r) = \frac{1}{3\pi r_\mathrm{e}^3 r_\mathrm{max}}\left(\frac{r}{r_\mathrm{max}}\right)^{-\frac{2}{3}} \quad \text{(S22)}$$

To replicate experimental conditions on PIPS in this work, we set T_v=60 °C, ΔT=1°C, constant θ_a=110°, and varied contact angle hysteresis (cosθ_r-cosθ_a). The contact angle hysteresis in this model serves primarily to increase r_{max} (Figure S8a), which in turn reduces the heat transfer coefficient (Figure S8b). Because subcool was set as a constant, this effect also results in a change in heat flux, shown as the left axis of Figure S8b. Measured contact angle hysteresis and r_{max} of the PIPS surfaces tested in this work are also included in the figures. The level of change observed in this work, shown in Table S3 and plotted directly on Figure S8a, is not expected to affect performance significantly, however, continued increase to the contact angle hysteresis would result in an observable change.

Furthermore, our modeling suggests that other factors may also have an observable effect on the heat transfer performance, notably, the condensate nucleation density, N_s, which influences r_e. Figure S9 shows the heat transfer coefficient and heat flux predicted by the model while varying r_e. Note that the curves overlap given the surface subcool was set at a constant value of 1 °C. The effect of r_e is significant and may contribute to differences in the heat transfer coefficient of the

different PIPS surfaces tested, as well as in changes observed over time during durability and degradation testing on a particular surface.

S5. Corrosion Resistance

Because PIPS coatings are primarily non-reactive, low-surface-energy polymer at their outermost surface, they reduce surface corrosion significantly. In Figure S5, the potentiodynamic polarization curves for bare copper, CuO nanoblade PIPS, and Cu nanowire PIPS with φ = 0.4, measured in 3.5 weight percent NaCl solution are shown. Using Tafel extrapolation, the corrosion current, I_{corr}, can be determined. This current was then used to determine the corrosion rate, *CR*, of the surfaces as

$$CR = \frac{I_{corr} K \cdot EW}{\rho A} \tag{S23}$$

where *K* is a constant that defines the units of corrosion rate (*K* = 3272 mm/A-cm-year to find corrosion rate in mm/year), *EW* is the equivalent weight of the copper, ρ is the density, and *A* is the area of the tested surface. The corresponding corrosion rates are shown in Table S2. The corrosion rate of CuO nanoblade PIPS was more than two orders of magnitude less than a bare copper surface, providing significant surface protection. The higher corrosion rate of Cu nanowire PIPS may have contributed to the larger increase of contact angle hysteresis during continuous condensation testing.

S6. Uncertainty Propagation

This section presents the method used for uncertainty propagation of the experimental results. The method for determining uncertainty is described in NIST Technical Note 1297.[16] Individual

measurements were assumed to be uncorrelated and random. Therefore, the uncertainty, U, in a calculated quantity, Y, is determined as

$$U = \sqrt{\sum_i \left(\frac{\partial Y}{\partial X_i}\right)^2 U_x^2} \tag{S24}$$

where X is the measured variable, and U_x is the uncertainty in the measured variable. Table S4 summarizes the uncertainty associated with each experimental measurement that was then propagated according to Equation S24 to determine uncertainty.

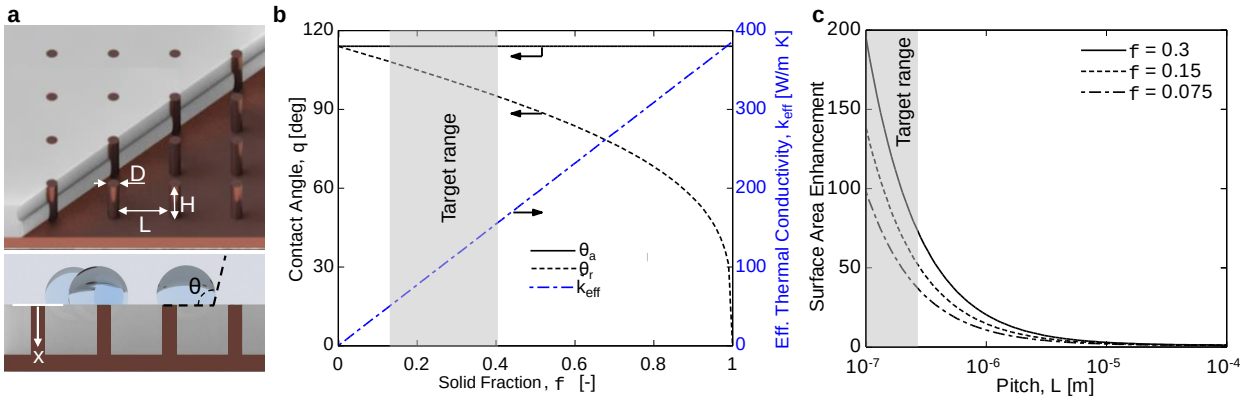

Figure S1: Design of PIPS. a, Schematic of PIPS. Structured surfaces (depicted with pillars in the schematic) are infused with polymer (white material in schematic). A portion of the polymer was removed in the schematic to reveal the structured surface with characteristic dimensions height, *H*, diameter, *D*, and pitch, *L*. **b**, Effective thermal conductivity of the coating (dashed blue line) as well as predicted advancing and receding contact angles (black lines) of the surface. **c**, Surface area enhancement for a surface with pillars and $H = 10$ μm and different nanostructure solid fractions, φ, as structure pitch is varied. Structure diameter was also varied to maintain constant nanostructure solid fraction.

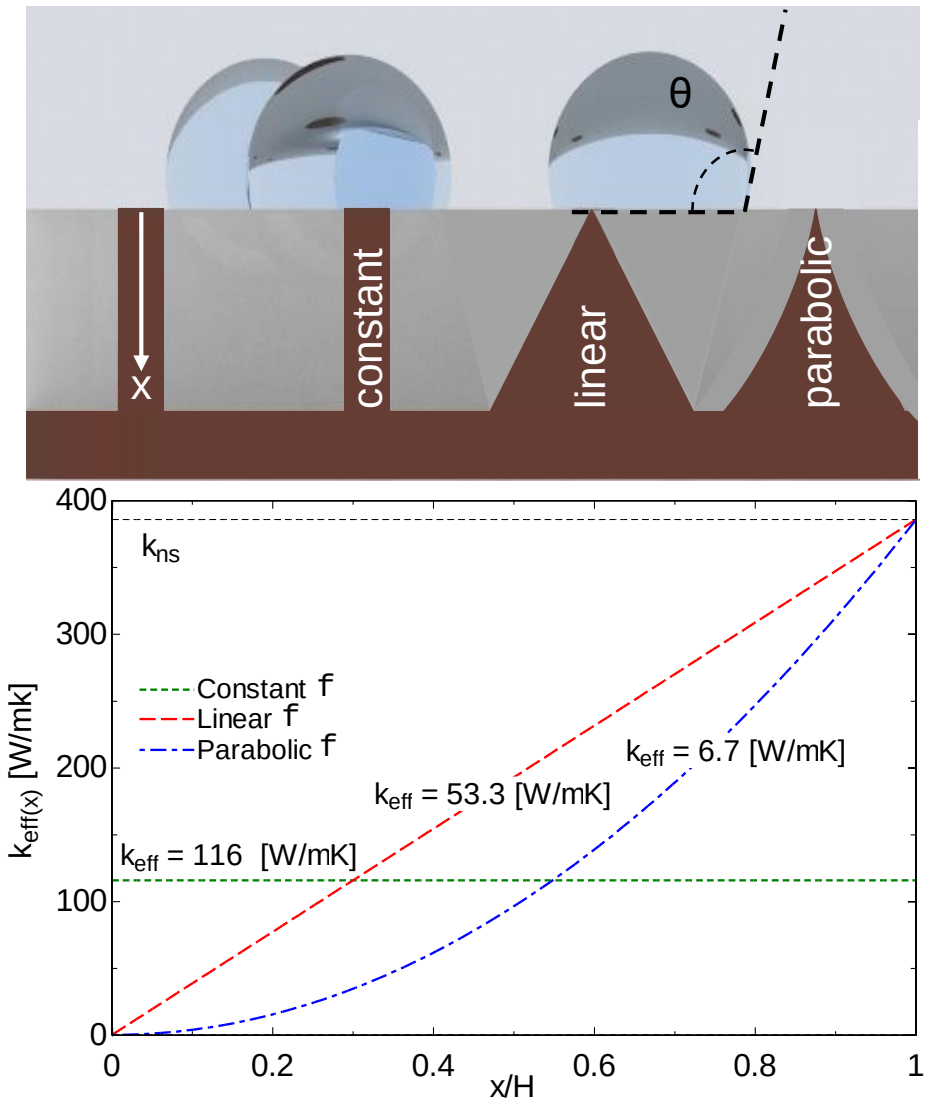

Figure S2: Effect of variable nanostructure solid fraction on effective thermal conductivity. Three cases for variable nanostructure solid fraction along x are considered. Constant solid fraction, such as pillars, linear solid fraction, such as triangular ridges, and parabolic solid fraction, such as cones. For simplicity, the linear and parabolic cases are assumed to go from $\phi = 0$ at $x = 0$ to $\phi = 1$ at $x = H$, whereas the constant solid fraction in this figure is 0.3. The resulting $k_{eff}(x)$ is shown, and the resulting overall k_{eff}, *i.e.*, the effective thermal conductivity of the layer assuming it were homogeneous, is calculated and labeled in the figure.

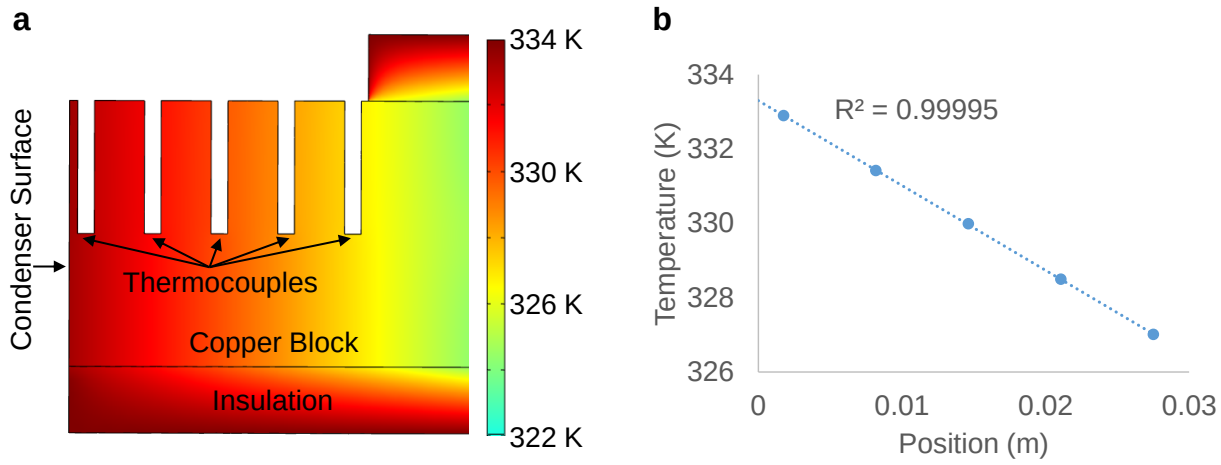

Figure S3: a, COMSOL model of the condenser block with an applied heat flux of ~100,000 W/m^2 and a condensation heat transfer coefficient of 120,000 W/m^{2}K to represent the performance of PIPS. **b**, The resulting temperature profile is highly linear, validating this measurement strategy. Points are the temperature at the thermocouples.

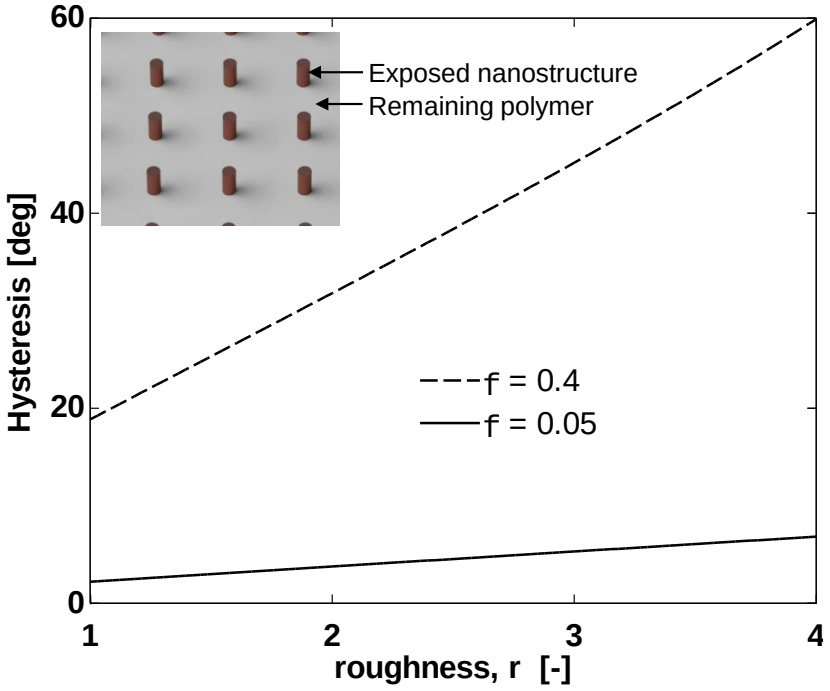

Figure S4: Contact angle hysteresis as the surface roughness increases (*i.e.*, nanostructures are exposed due to gradual polymer removal) for a nanostructure solid fraction of 0.4 and 0.05. Due to the larger nanostructure solid fraction at the surface of Cu Nanowire PIPS, the hysteresis grows more rapidly with removal of the polymer. We attribute the larger solid fraction to be the primary reason that an increase in the contact angle hysteresis was observed for the Cu Nanowire PIPS and not the CuO Nanoblade PIPS.

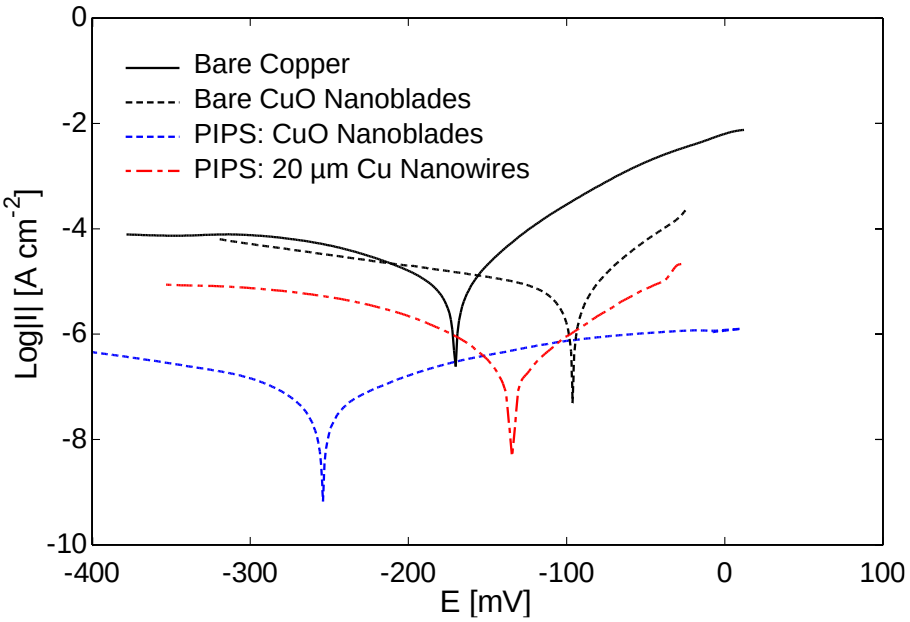

Figure S5: Potentiodynamic polarization curves for bare copper and PIPS, measured in 3.5 weight percent NaCl solution. Corrosion rate on PIPS was reduced two orders of magnitude.

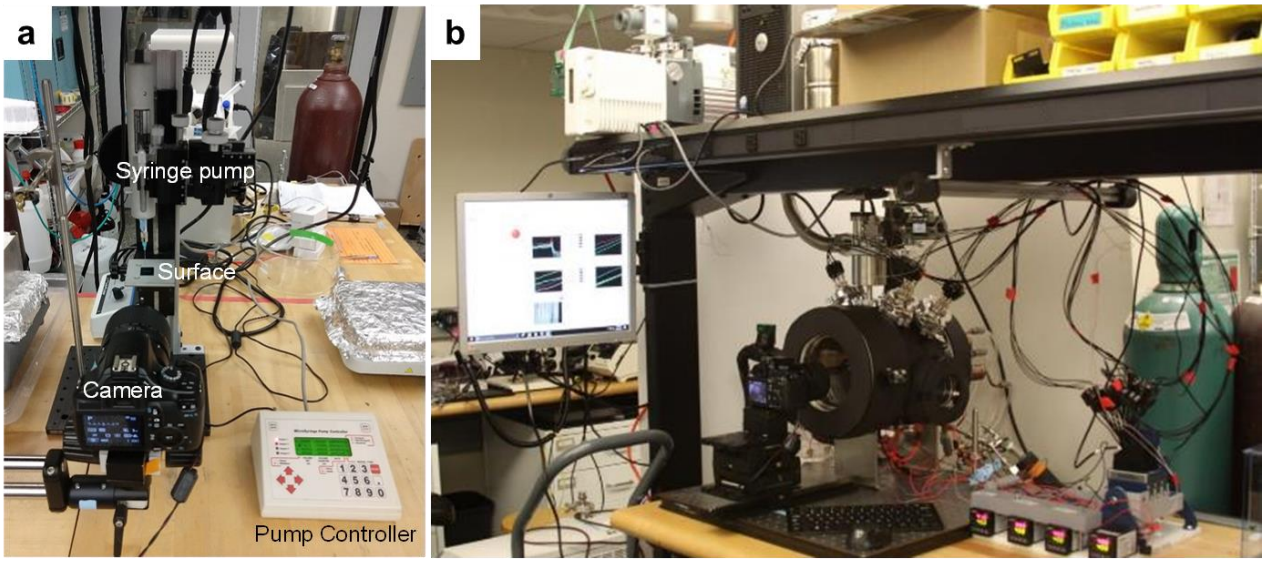

Figure S6: Experimental setups a. Contact angle measurement. Image of the custom-built contact angle measurement setup. A syringe added and removed liquid from a droplet on the surface while a camera recorded the contact angle. A light source (not shown) provided illumination of the droplet. **b.** Environmental chamber for heat transfer and durability measurements.

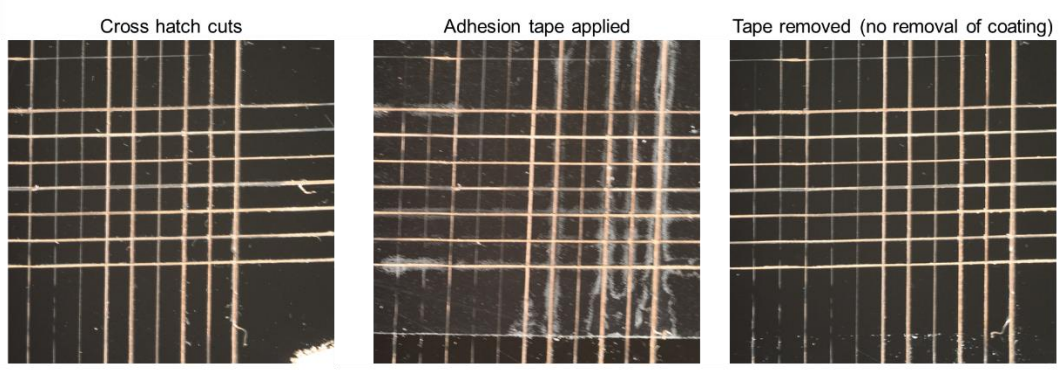

Figure S7: Cross hatch adhesion testing on CuO PIPS, showing no removal of the layer during the test. This qualitative test suggests high adhesion of PIPS.

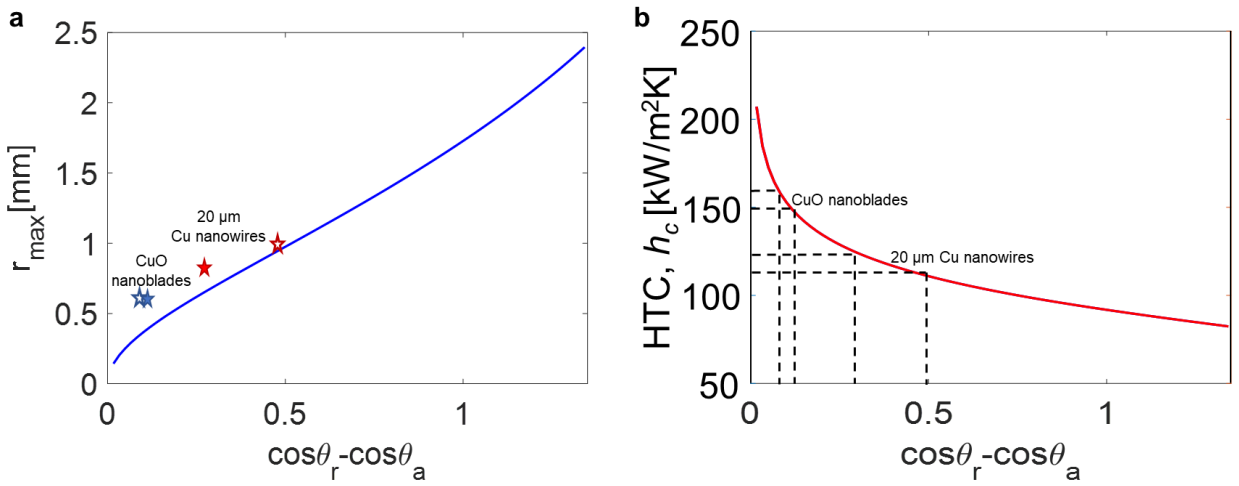

Figure S8: a, The predicted maximum droplet size, r_{max}, expected on the condensing surfaces as a function of the contact angle hysteresis. The stars represent the observed r_{max}, extracted from videos of condensation on the surfaces, at the beginning (filled star) and end (open star) of the continuous condensation experiments for the CuO nanoblade PIPS (blue stars) and the Cu nanowire surface (red stars). **b**, A change in contact angle hysteresis results in a change in the expected heat transfer coefficient due to the change in droplet departure size. The observed changes during durability testing in this work only suggest a moderate change to the expected heat transfer coefficient (<10%). However, continued degradation and the corresponding increase in hysteresis would be expected to observably change heat transfer performance.

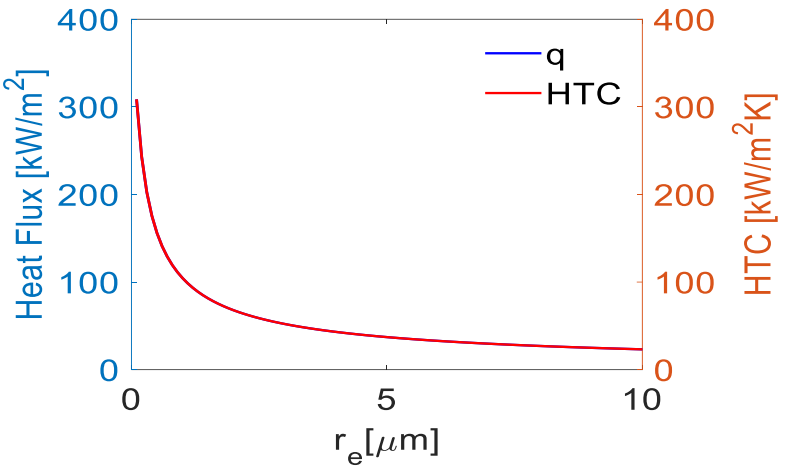

Figure S9: Modeled heat flux and heat transfer coefficient as a function of r_e. The expected heat transfer performance decreases as r_e increases. Note that the curves overlap given the surface subcool was set at a constant value of 1 °C.

Table S1: Critical thickness, effective thermal conductivity, and expected contact angle hysteresis. Different possible nanostructure type, materials, and designs were considered. The resulting critical thickness, effective thermal conductivity, surface nanostructure solid fraction, and expected advancing and receding contact angles are shown. Critical thickness is the thickness at which the thermal resistance of the composite hydrophobic layer is expected to reduce condensation heat transfer by 10%. Because of the lower thermal conductivity of copper oxide, the critical thickness of designs using copper oxide was considerably less than copper, but still a large improvement over polymer only. The predicted effective thermal conductivities are consistent with literature for similar composites.[17,18] Highlighted in blue are designs that were chosen for this study.

Nanostructure Type	**Material**	H_{crit} **[µm]**	k_{eff} **[W/mK]**	$\phi(x=0)$	θ_a **[deg]**	θ_r **[deg]**
None (Teflon AF)	-	0.22	0.29	0	114	114
Parabolic	Copper	4.96	6.60	0	114	114
Linear	Copper	39.10	52.00	0	114	114
Constant	Copper	42.56	56.60	0.15	114	107.3
Constant	Copper	116.32	154.70	0.4	114	95.1
Parabolic	Copper Oxide	1.15	1.53	0	114	114
Constant	Copper Oxide	2.41	3.21	0.15	114	107.3

Table S2: Corrosion current and rate of copper and copper oxide nanoblade PIPS.

Surface	I_{corr} (A/cm^2)	CR (mm/year)
Bare Copper	1.08E-5	0.25
Bare CuO	6.31E-6	0.15
PIPS: CuO Nanoblade	8.17E-8	0.0019
PIPS: 20 µm Cu Nanowire	1.58E-7	0.0036

Table S3: Advancing and receding contact angles of PIPS surfaces before and after durability testing, along with the observed maximum droplet departure diameter. These values are plotted directly into Figure S8a.

PIPS	θ_a (deg)	θ_r (deg)	$\cos\theta_r - \cos\theta_a$	r_{max} [mm]
Cu Nanowire (0 hr)	105.1	89	0.28	0.838
Cu Nanowire (4800 hr)	110	81.5	0.49	1.18
CuO Nanoblade (0 hr)	108.2	103.2	0.08	0.634
CuO Nanoblade (4800 hr)	108.2	101.3	0.12	0.61

Table S4: Uncertainties corresponding to experimental measurements. Standard deviation in vapor temperature was primarily caused by fluctuations in the chamber conditions due to PID control of heaters and chillers, as opposed to the measurement *via* thermocouples. Thermocouples were calibrated before testing to reduce uncertainty on the measurement. The uncertainty in the contact angle was primarily a result of the contact angle measurement and imaging setup, given the setup does not precisely control the surface orientation relative to the camera, nor uses a collimated light source, leading to uncertainty when extracting the contact angle from images.

Experimental Measurement	Uncertainty/standard deviation
Steam vapor temperature standard deviation in environmental chamber	1.4 °C
Contact angle measurement (θ) uncertainty	5 degrees
Calibrated J-type thermocouples uncertainty	0.1 °C

Video Captions

Video S1. Dropwise condensation on CuO nanoblade PIPS on the first day of durability testing at 60 °C with 100 kW/m^2 heat flux. Playback speed is real time.

Video S2. Dropwise condensation on CuO nanoblade PIPS after 200 days of durability testing at 60 °C with 100 kW/m^2 heat flux. Playback speed is real time.

Video S3. Dropwise condensation on Cu nanowire PIPS on the first day of durability testing at 60 °C with 100 kW/m^2 heat flux. Playback speed is real time.

Video S4. Dropwise condensation on Cu nanowire PIPS after 200 days of durability testing at 60 °C with 100 kW/m^2 heat flux. Playback speed is real time.

References

1. Neumann, A.; Abdelmessih, A.; Hameed, A. The Role of Contact Angles and Contact Angle Hysteresis in Dropwise Condensation Heat Transfer. *Int. J. Heat Mass Transfer* **1978,** *21*, 947-953.

2. Choi, W.; Tuteja, A.; Mabry, J. M.; Cohen, R. E.; McKinley, G. H. A Modified Cassie–Baxter Relationship to Explain Contact Angle Hysteresis and Anisotropy on Non-Wetting Textured Surfaces. *J. Colloid Interface Sci.* **2009,** *339*, 208-216.

3. Burger, N.; Laachachi, A.; Ferriol, M.; Lutz, M.; Toniazzo, V.; Ruch, D. Review of Thermal Conductivity in Composites: Mechanisms, Parameters and Theory. *Prog. Polym. Sci.* **2016,** *61*, 1-28.

4. Mantle, W. J.; Chang, W. S. Effective Thermal Conductivity of Sintered Metal Fibers. *J. Thermophys. Heat Transfer* **1991,** *5*, 545-549.

5. Singh, B.; Dybbs, A.; Lyman, F. Experimental Study of the Effective Thermal Conductivity of Liquid Saturated Sintered Fiber Metal Wicks. *Int. J. Heat Mass Transfer* **1973,** *16*, 145-155.

6. Wu, S. Modifications of Polymer Surfaces: Mechanisms of Wettability and Bondability Improvements. In *Polymer Interface and Adhesion*, Taylor & Francis Group: New York, 1982; pp 279-336.

7. Comyn, J. Surface Treatment for Adhesion, and for Abhesion. In *Adhesion Science*, Royal Society of Chemistry: Cambridge, 1997; pp 18-25.

8. Awaja, F.; Gilbert, M.; Kelly, G.; Fox, B.; Pigram, P. J. Adhesion of Polymers. *Prog. Polym. Sci.* **2009,** *34*, 948-968.

9. Rose, J. Dropwise Condensation Theory and Experiment: A Review. *Proc. Inst. Mech. Eng., Part A* **2002,** *216*, 115-128.

10. Enright, R.; Miljkovic, N.; Dou, N.; Nam, Y.; Wang, E. N. Condensation on Superhydrophobic Copper Oxide Nanostructures. *J. Heat Transfer* **2013,** *135*, 091304.

11. Kim, S.; Kim, K. J. Dropwise Condensation Modeling Suitable for Superhydrophobic Surfaces. *J. Heat Transfer* **2011,** *133*.

12. Miljkovic, N.; Enright, R.; Wang, E. N. Modeling and Optimization of Superhydrophobic Condensation. *J. Heat Transfer* **2013,** *135*.

13. Carey, V. P. External Condensation. In *Liquid Vapor Phase Change Phenomena*. 2nd ed.; Taylor & Francis: New York, NY 2008; pp 391-446.

14. Liu, X.; Cheng, P. Dropwise Condensation Theory Revisited Part II. Droplet Nucleation Density and Condensation Heat Flux. *Int. J. Heat Mass Transfer* **2015,** *83*, 842-849.

15. Le Fevre, E. J.; Rose, J. W. A Theory of Heat Transfer by Dropwise Condensation. *Proc. Third Int. Heat Transfer Conf.* **1966**, 362-375.

16. Taylor, B. N.; Kuyatt, C. E. Guidelines for Evaluating and Expressing the Uncertainty of Nist Measurement Results. In *NIST Technical Note 1297*, 1994 ed.; U.S. Government Printing Office: Washington DC, 1994; pp 1-20.

17. Chang, H. C.; Rajagopal, M. C.; Hoque, M. J.; Oh, J.; Li, L.; Li, J.; Zhao, H.; Kuntumalla, G.; Sundar, S.; Meng, Y. Composite Structured Surfaces for Durable Dropwise Condensation. *Int. J. Heat Mass Transfer* **2020**, 119890.

18. Barako, M. T.; Isaacson, S. G.; Lian, F.; Pop, E.; Dauskardt, R. H.; Goodson, K. E.; Tice, J. Dense Vertically Aligned Copper Nanowire Composites as High Performance Thermal Interface Materials. *ACS Appl. Mater. Interfaces* **2017,** *9*, 42067-42074.